Nano Research Energy

ISSN 2791-0091 (print); 2790-8119 (online)
https://doi.org/10.26599/NRE.2025.9120182

Research Article

Non-metal anion doping construction of the durable cathode with optimized oxygen vacancies in aqueous zinc-ion batteries

Huiying Gao[1], Jinfeng Xie[2], Shirui Zhang[1], Chengjia Mei[2], Jun Liu[2], Haiqiong Du[2], Chengsi Zhao[1], Weihai Ni[1], He Huang[2] (✉), and Qi Xue[1] (✉)

[1] School of Physical Science and Technology, Soochow University, Suzhou 215006, China
[2] School of Optoelectronic Science and Engineering, Soochow University, Suzhou 215006, China

Received: 9 May 2025 / **Revised:** 29 May 2025 / **Accepted:** 4 June 2025 / **Published date:** 1 August 2025

ABSTRACT

Aqueous zinc-ion batteries have already shown promising prospects in electronic devices, owing to their environmentally benign nature and high safety. Manganese dioxide is studied as one kind of cathode material, however, it typically displays slow kinetics and unstable crystal structures. Defect engineering introduces active sites in MnO_2, while metal ion doping increases material's molar mass, which offers rare zinc storage contribution. To find a feasible doping strategy with optimized oxygen vacancies is highly desirable. Herein, the incorporation of nitrogen-doped MnO_2 (NMO) with lower electronegativity as the cathode enabled the realization of reversible aqueous zinc-ion batteries. The structural stability and electrochemical properties of NMO were enhanced by nitrogen doping. NMO exhibited a smaller charge transfer resistance than pristine MnO_2 (279.6 Ω vs. 484.5 Ω). Cyclic voltammetry curves displayed that the incorporation of nitrogen doping could decrease the polarization, which provided a good basis for optimizing electrode kinetics. Specifically, the battery displayed a promising specific discharge capacity of 153.1 $mAh \cdot g^{-1}$ at 0.5 $A \cdot g^{-1}$ after 100 cycles. And at the current density of 1 $A \cdot g^{-1}$, the capacity retention of NMO after 1600 cycles was 1.72 times that of pristine MnO_2. This study proposed a feasible idea for modifying non-metal hole sites in the cathode materials of zinc-based batteries, providing deep insights for future practical application of energy storage systems.

KEYWORDS

anionic doping, manganese dioxide, zinc-ion battery

1 Introduction

Decades of global energy structure optimization efforts have intensified the urgency of energy development [1, 2]. Although the lithium-ion batteries receive tremendous interest in rechargeable energy storage system, resource constraints and flammable organic electrolytes seriously hinder their applications [3–5]. The above limitations accelerate the industrialization of frontier energy storage devices. Therefore, aqueous Zn^{2+}-based battery systems employing two-electron redox mechanisms with the merits of intrinsic safety, economic viability, favorable theoretical capacity and environmental friendliness have obtained widespread attention [6–9].

Due to the prospective application of Zn-based aqueous batteries, advancing pivotal components remains crucial, notably innovating cathode materials with superior performance [10–12]. Among them, MnO_2, featuring a significant theoretical capacity of 308 $mAh \cdot g^{-1}$ and possessing hypotoxicity, has garnered increasing attention [13–18]. Nevertheless, the considerable ionic radius of hydrated cations induces intense coulombic interactions with the host during the charge/discharge process of the battery [19]. These interactions lead to cation clusters in the tunnels, which block ion diffusion pathways and reduce the ionic conductivity. Furthermore, the Jahn-Teller effect accelerates the decomposition of the cathode, leading to unsatisfactory cycling performance [19–22]. Doping is regarded as one of the most efficient approaches. Metal ion doping with Mg, Fe, Al, K, Co, Cu, and Mo was suggested in earlier reports [23–30]. Metal ions can effectively increase the electron conductivity, so that the electrochemical properties of manganese dioxide could be enhanced. Unfortunately, metal ion doping increases the material's molar mass, and metal ion doping processes usually require complicated treatment [19]. Accordingly, oxygen vacancies could introduce more active sites, which facilitate zinc ions undergoing rapid oxidation-reduction, strengthening the pseudocapacitance contribution, thereby increasing the capacity [31–35]. However, the introduced vacancies also easily tend to transform the MnO_2 phase [36, 37]. Anionic doping partially counterbalances the charge imbalance caused by oxygen vacancies, thereby reducing structural stress [38–40]. To overcome this challenge, anion doping (such as S, F, C) serves as a feasible strategy for optimizing charge storage efficiency and structural stability of electrodes in a

Address correspondence to He Huang, hh@suda.edu.cn; Qi Xue, xq@suda.edu.cn

battery [40–42]. The addition of N anions can broaden the tunnel spacing and provide a buffer against the volume expansion and structural deformation of the electrode during cycling [43]. So far, however, limited attention has been paid to the synergistic benefit of anion and oxygen vacancy; the work in this area is not comprehensive enough. In light of the above issues, constructing the synergy between anions with smaller molar mass and oxygen vacancies for adjusting the surface electric environment of the Mn-O bond is important and urgent.

Herein, a low-valence manganese oxide was engineered via low-temperature synthesis for durable electrodes in zinc-ion battery. The as-prepared nitrogen-doped MnO_2(NMO) retained impressive performance of 153.1 mAh·g^{-1} after 100 cycles at 0.5 A·g^{-1}. Moreover, following 1600 cycles at 1 A·g^{-1}, NMO sustained a specific capacity of 83.1 mAh·g^{-1}, reaching approximately twice that of pristine MnO_2. Electrochemical analysis affirmed that the incorporation of nitrogen doping could decrease the polarization and reverse the unfavorable Jahn-Teller effect. With the rapid interband transition of lone-pair electrons, the conductivity of cathode materials was effectively improved. Benefiting from the synergy of the oxygen vacancy and nitrogen-doping within the cathode material, the stability of the battery was effectively optimized, and the transmission dynamics of the inherent structure was improved. This work revealed the potential application of anion doping in the cathode materials for aqueous zinc-ion batteries, thereby opening new avenues for energy storage development.

2 Experimental

2.1 Materials

Chemicals and solutions were directly utilized as-received: Potassium permanganate ($KMnO_4$, 99.5%, Sinopharm), Manganese sulfate ($MnSO_4$, 98%, Adamas), Ammonium bicarbonate (NH_4HCO_3, 99.995%, Aladdin), Acetylene black (ACET, 99.9%, Kluthe), Polyvinylidene fluoride (PVDF, 99.5%, Arkema), 1-Methyl-2-pyrrolidinone (NMP, 99.0%, Aladdin).

2.2 Preparation of materials

The α-MnO_2 cathode material was obtained through the utilization of a common hydrothermal reaction approach. Briefly, deionized (DI) water was used to completely dissolve the powders of $KMnO_4$ and $MnSO_4$, respectively, to form homogeneous solutions for further treatment. Then, the $KMnO_4$ solution was vigorously mixed with the $MnSO_4$ solution using a stirrer. The above sample was then solvothermally treated at 160 °C for 12 hours under autogenous pressure conditions in a 100 mL autoclave equipped with a Teflon liner. The reaction is formulated in the following reaction:

$$3MnSO_4 + 2KMnO_4 + 2H_2O \rightarrow 5MnO_2 + K_2SO_4 + 2H_2SO_4$$

After the autoclave naturally cooled to ambient conditions, the precipitate underwent cyclic washing with DI water (centrifugation-redispersion) until the pH value reached approximately 7.0, ensuring the elimination of a large number of residual soluble ions. Subsequently, it was dried under vacuum at 60 °C overnight to generate a pure-phase material.

The nitrogen-doped manganese oxide cathode was synthesized in the furnace by annealing. In detail, the alumina combustion boat loaded with ammonium salts was positioned in the upstream zone of the tubular furnace, while the MnO_2-containing counterpart was situated downstream. The MnO_2 nanorods were annealed at 200 °C, along the gas flow direction (30 sccm N_2), and the resulting nitrogen-doped MnO_2 samples were named as NMO.

2.3 Electrode assembly

The electrode slurry was fabricated through the following process: the NMO/MnO_2 powder (70 wt.%), ACET (20 wt.%), and PVDF (10 wt.%) were thoroughly blended together in 500 μL NMP. Then, the electrode slurry was blade-coated onto Ti foil (0.03 mm thickness) and vacuum-dried at 60 °C overnight to fabricate working electrodes with 1–2 mg active material loading. A Ti foil (diameter=12 mm) was used as the cathode, and zinc foil (16 mm) was used as an anode. The electrolyte formulation (100 μL) was prepared using DI water, dissolving $ZnSO_4$ (1.0 mol) and $MnSO_4$ (0.1 mol). A glass fiber separator (Whatman GF/D, 19 mm diameter) was utilized. Assemble the CR 2032 type coin cell under ambient air conditions.

2.4 Material characterization

We dispersed the powder sample in alcohol, and then dropped it onto a clean silicon wafer and a copper mesh. A scanning electron microscope (SEM, Hitachi Regulus 8100, 10 keV) was used to conduct a simple morphological analysis of the sample on the silicon wafer. We tested the sample on the copper mesh to get TEM images adopting a high-resolution transmission electron microscope (HRTEM, Thermo Scientific Talos F200X G2) loaded with an energy dispersive spectroscopy (EDS) for obtaining the material structure, crystal plane information, and the distribution pattern of elements. Powder specimens (200 mesh) were loaded into a quartz sample cell and tested by X-ray diffraction (XRD) using a Bruker D8 ADVANCE system (λ_{Cu} Kα=1.5418 Å, 40 kV, 40 mA, Germany) with scans from 10° to 80° (2θ) at 0.01° increments. Powder specimens were dispersed on glass substrates (1 mm thickness) for Raman spectroscopy (Horiba, Xplora Plus, 532 nm laser, 50× objective). The powder specimens were fixed on an indium foil substrate and subjected to X-ray photoelectron spectroscopy (XPS) analysis (Kratos, AXIS Ultra DLD) for elemental and valence state determination.

2.5 Electrochemical performance testing

The performance metrics of the as-prepared sample were measured through a coin cell test system. Cyclic voltammetry (CV, 0.9–1.8 V) tests were applied to record the variation of current with respect to electrode potential, thereby determining the chemical reversibility and stability of the electrode reactions. The electrochemical impedance spectroscopy tests (EIS, 0.01–10 kHz) was utilized to investigate the kinetic properties of the electrode processes (CHI 760e, Shanghai, China). Regarding the stability of as-fabricated samples, the cyclic stability of the electrode materials was evaluated by galvanostatic charge-discharge curves utilizing a battery testing system (LAND, CT3002A), and then the rapid charge-discharge capabilities of the electrode materials were assessed through rate performance tests.

3 Results and discussion

Figure 1(a) reveals the hydrothermal-assisted nitrogen-doping strategy for synthesizing NMO nanorods. The initial MnO_2 nanorods were achieved through a conventional hydrothermal approach. Subsequently, NMO was prepared by a low-temperature doping method considering the thermal sensitivity of MnO_2. The SEM image (Fig. S1(a) in the Electronic

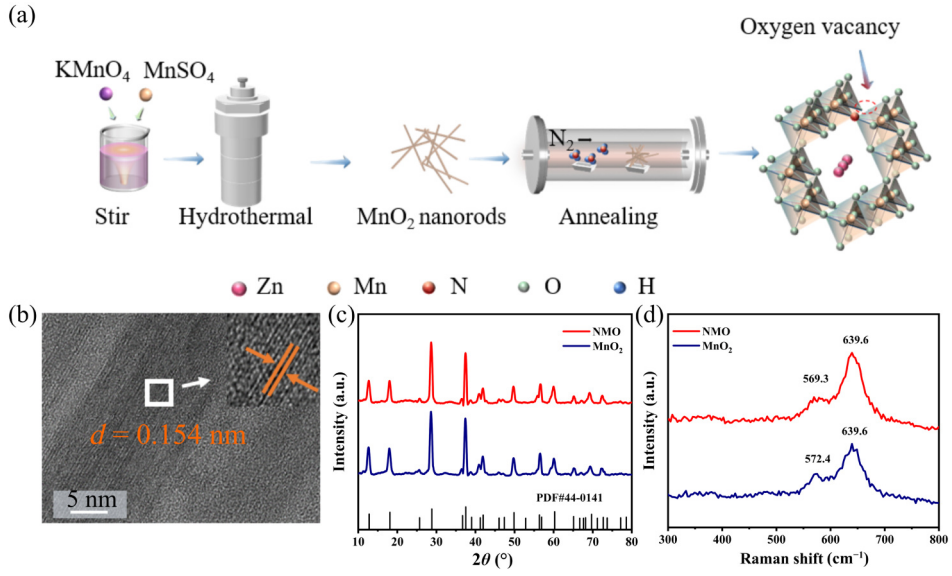

Figure 1 (a) Schematic illustration of the preparation workflow of NMO materials; (b) HRTEM image of NMO; (c) XRD patterns of the corresponding materials; (d) Raman spectrum of NMO and MnO_2 samples.

Supplementary Material (ESM)) shows that the pristine MnO_2 present uniform micrometer-scale rod structures. The sample of NMO after annealing demonstrated the same rod-like structure as the pristine MnO_2, as shown in Fig. S1(b) in the ESM, the impact of low-temperature doping was negligible on the nanostructure of MnO_2. In addition, HRTEM images analysis confirmed the (521) plane in both MnO_2 and NMO, with MnO_2, exhibiting an interlayer spacing of 0.148 nm (Fig. S1(c) in the ESM) [43, 44]. NMO displayed lattice with interlayer spacing of 0.154 nm (Fig. 1(b)), representing a slight increase in the lattice resulting from nitrogen doping in MnO_2 [44]. This result also showed that low-temperature doping effectively prevented structure changing [45, 46]. The XRD patterns of MnO_2 and NMO showed precise alignment with the standard tetragonal phase (PDF#44-0141) [44, 47]. In terms of the XRD results, the diffraction peaks of MnO_2 at 12.7°, 18.0°, 28.6°, 37.5°, and 60.1° matched well with the (110), (200), (310), (211), and (521) crystal planes of MnO_2 (Fig. 1(c)). Post-annealing XRD analysis confirmed that NMO maintains well-defined diffraction patterns characteristic of α-MnO_2 [23]. Consequently, N-doping exhibited negligible alteration to the MnO_2 lattice structure. Compared to unmodified MnO_2, the peak intensity of NMO was slightly decreased. According to previous reports, low crystallinity exhibited a high density of grain boundaries [48]. Through atomic rearrangement, ion diffusion pathways were established, thereby enhancing the efficiency of the electrochemical reaction. It should be emphasized that in Fig. S2 in the ESM, the (310) peak of NMO shifted to the lower angle, which, based on Bragg's law, indicating the expansion of the NMO was larger, and further promoting the rapid diffusion of Zn^{2+}. The formation of covalent N-Mn bonds during annealing process mitigated the strong electrostatic repulsion, thereby inducing lattice expansion through controlled MnO_2 bond elongation. The structure and the property of NMO and MnO_2 materials were further comprehensively studied by Raman and XPS spectra. As revealed in Fig. 1(d), both NMO and MnO_2 exhibited similar peaks. After doping, the peaks confirmed the integrity of the MnO_6 octahedral tunnel structure [23, 44]. The tensile vibration of MnO_2's Mn-O bond could be observed at 572.4 cm^{-1}; however, the Raman peak of NMO shifted to 569.3 cm^{-1}, and this peak shift confirmed the nitrogen incorporation into oxygen vacancies during annealing [19, 45, 49]. These results indicated that nitrogen doping does not affect crystal morphology. The composition distribution of NMO was further analyzed through EDS element mapping (Figs. S3(a)-3(d) in the ESM), demonstrating uniform distribution of various elements throughout NMO samples.

As shown in Fig. 2(a), compared with pristine MnO_2, the N element signal appeared in the full X-ray photoelectron spectrum of the NMO. A distinct N 1s spectral signature emerged in the XPS profile of NMO (Fig. 2(b)), with this characteristic peak aligning with Mn-N bond (399.9 eV) coordination [45]. The N 1s spectra further suggested the successful doping of nitrogen in the NMO samples [45]. As illustrated in Fig. 2(c), the shift of Mn 2p peaks of NMO and MnO_2 samples can be clearly observed. For NMO and MnO_2, the spin energy differences were 11.80 and 11.86 eV, respectively. The Mn 2p peak of NMO shifted, the same trend was displayed on the peaks of O 1s. Additionally, compared to MnO_2, notable shift of Mn 3s binding energies toward higher values was observed in NMO with the splitting energy widening from 4.7 to 5.6 eV (Fig. S4 in the ESM). Combined with the Mn 2p spectra, which illustrated a charge redistribution of the structure. Reducing the valence of manganese oxide was beneficial to prevent the electrode from side reactions with oxygen at high potential in the discharge process [50]. This shift indicated that some electrons were transferred to N atoms, resulting in the local accumulation of electrons at the N-coordination sites, thus confirming the Mn-N covalent interaction. The formation of N-Mn might induce charge redistribution in the material, leading to changes in electronic structure and electrical conductivity [51, 52]. Simultaneously, modifications in the band structure could occur, which will directly affect the bandgap of the material [53]. Regarding the N-doping via a nitrogen plasma strategy, DFT calculations results demonstrated that the charge density decreased from 0.996 to 0.372, indicating electronics incline to gather to the N atom [53]. In Fig. 2(d), O 1s spectra were deconstructed into two distinguishable parts. The part labeled as Mn-O had a binding energy of 529.7 eV, whereas oxygen vacancy featured a binding energy of 531.2 eV [23, 51, 53, 54]. Compared to MnO_2, NMO exhibited a significant reduction in oxygen vacancy concentration, directly evidencing nitrogen-mediated vacancy compensation during annealing.

To comprehensively investigate the electrochemical

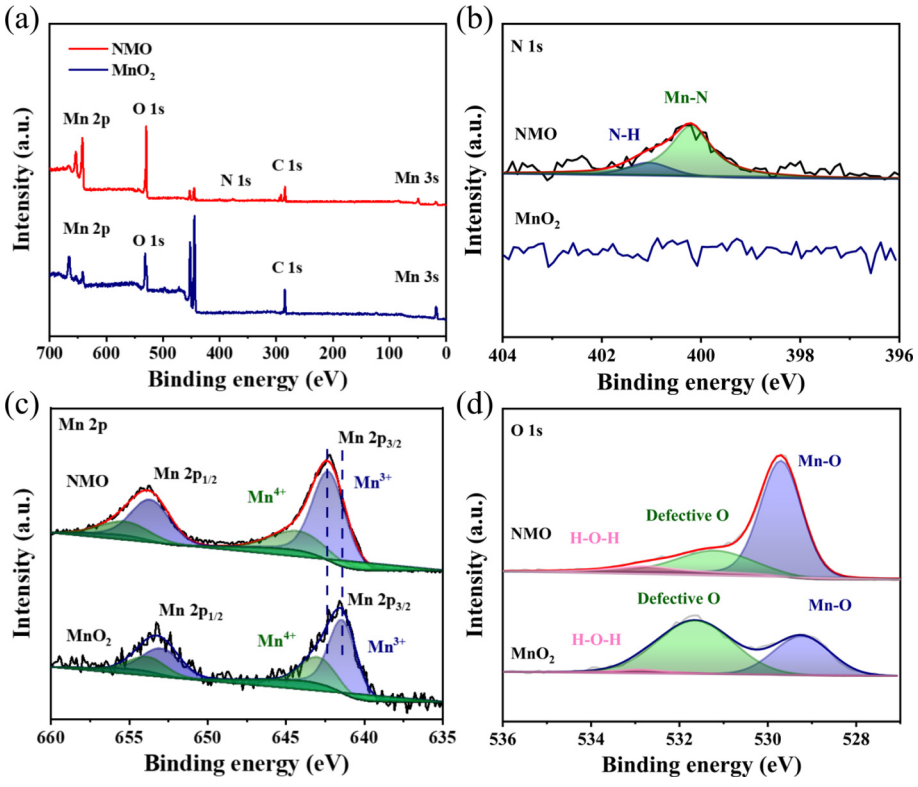

Figure 2 Element identification of the as-prepared samples. (a) XPS full spectrum of NMO and MnO_2. XPS investigation of N 1s (b), Mn 2p (c), and O 1s (d), of the corresponding samples.

performance of the NMO and MnO_2 cathodes in aqueous zinc ion battery, the coin-type batteries were introduced. Electrochemical profiles of MnO_2 and NMO were assessed via CV curves (scan rate at 0.5 $mV \cdot s^{-1}$) under test window of 0.9–1.8 V (vs. Zn/Zn^{2+}). As presented in Fig. 3(a), the CV results of the Zn-NMO and Zn-MnO_2 cells reveal a comparable oxidation-reduction pattern. The reduction in peak potential difference in the CV graph indicated a significant improvement in the reversibility and kinetics of the Mn^{4+}/Mn^{3+} redox reaction [22, 54]. Specifically, two sets of electrochemical peaks were observable, aligning precisely with the findings from the dQ/dV curve depicted in Fig. S5 in the ESM. Notably, NMO exhibited higher current response, indicating enhanced electrochemical activity. The discharge cathodic behavior of NMO exhibited redox activity at 1.207 and 1.348 V, originating from Mn^{4+} reduction coupled with synergistic H^+/Zn^{2+} insertion during electrochemical cycling [22, 54]. The peak of 1.565 V and 1.631 V were related to the extraction of Zn^{2+} and H^+ from cathode materials and Mn^{3+}/Mn^{4+} redox transition. The disproportionation of Mn^{3+} might induce oxidation process of Mn^{2+} to Mn^{4+}. As exhibited in Fig. 3(a), the potential gaps of NMO were obviously smaller than the potential gaps of MnO_2, which indicated smaller polarization [19, 23]. The NMO cathode exhibited enhanced Zn^{2+} intercalation reversibility, validating its benign electrochemical activity and reaction kinetics. The galvanostatic charge/discharge behavior of both NMO and pristine sample at a current density of 0.1 $A \cdot g^{-1}$ was comparatively analyzed (Fig. S6 in the ESM). This curve was very consistent with the CV curve. The two distinct voltage plateaus were clearly observed during the cycling process, aligning with the result in the CV profiles (1.318 V/1.565 V and 1.307 V/1.567 V). Meanwhile, NMO exhibited a discharge/charge capacity of 290.8/312.7 $mAh \cdot g^{-1}$, higher than MnO_2 (268.1/292.6 $mAh \cdot g^{-1}$). Compared with MnO_2, nitrogen doping could decrease the polarization, which provided a good basis for optimizing electrode kinetics, thereby enhancing the performance during cycling [19, 45]. To better understand the reaction dynamics of NMO and MnO_2 electrodes, an EIS test was characterized on NMO and MnO_2.

The Nyquist plot in Fig. 3(b) matched the equivalent circuit fitting results, showing that the charge transfer resistance decreased from 484.5 Ω (pristine MnO_2) to 279.6 Ω in NMO, and demonstrating improved charge transfer kinetics induced by nitrogen doping. Additionally, the slope in the low-frequency region corresponded to Warburg diffusion of ions in the electrode [16, 44]. The steeper slope of NMO compared to MnO_2 indicated faster diffusion kinetics. The result indicated that nitrogen doping within the MnO_2 served to decrease the bandgap width and elevate the material's electronic conductance [19, 45]. It was capable of efficiently diminishing the resistance associated with charge transfer and enhancing the mobility of both H^+ and Zn^{2+} ions, thereby optimizing the diffusion kinetics.

Figure S7 in the ESM presents the GCD profiles of NMO and MnO_2 electrodes under different testing parameters. The Zn^{2+} discharge plateau of NMO electrodes exhibited excellent stability. Specifically, even at 2 $A \cdot g^{-1}$, NMO electrodes maintained good capacity, thereby confirming its robust structural integrity. The rate capability of NMO and MnO_2 is shown in Fig. 3(c). Compared with the MnO_2 cathode, the capacities of NMO were 281.2, 264.4, 240.9, 225.4, and 218.4 $mAh \cdot g^{-1}$ at different rate. The NMO cathode maintained 272.5 $mAh \cdot g^{-1}$ at cycling rate restoration to 0.2 C, demonstrating that nitrogen-doping of MnO_2 cathode possessed pleasant rate performance and high reversibility. Comparative analysis of the NMO and MnO_2 electrode performance under 0.5 $A \cdot g^{-1}$ was presented in Fig. 3(d). Impressively, after undergoing 100 cycles, the NMO electrode retained a capacity of 153.1 $mAh \cdot g^{-1}$, and the corresponding coulombic efficiency is almost approaching 100%. Meanwhile, in Fig. S8 in the ESM, after 100 cycling tests, a small amount of by-

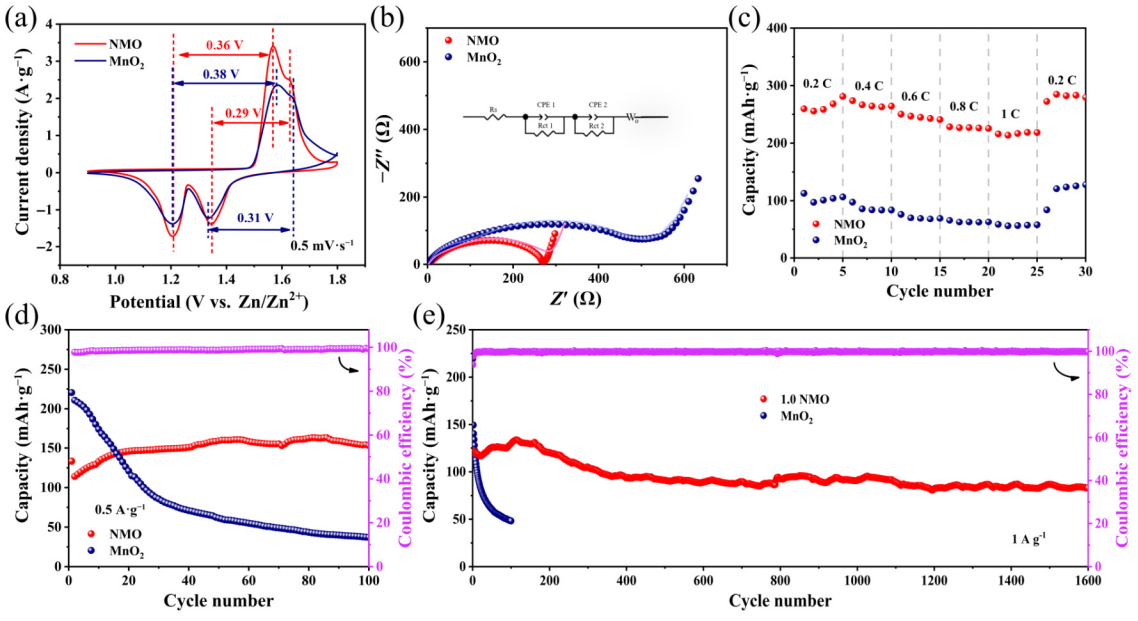

Figure 3 Electrochemical characteristics of NMO and MnO_2 electrodes. (a) CV data at current density of 0.5 mV·s^{-1}. (b) Nyquist plots. (c) Rate capability. (d) GCD cycling at current density of 0.5 A·g^{-1}. (e) Stability tests at current density of 1 A·g^{-1}.

products on the NMO electrode could be observed at the surface of the nanorods, but NMO also maintained its nanorod morphology, indicating pleasant structural stability. Conversely, MnO_2 with a beginning capacity of 220.5 mAh·g^{-1} underwent rapid fading after the 20th cycle, ultimately retaining only 37.1 mAh·g^{-1} after 100 cycles. This severe decay in performance indicated structural instability and inferior cycling performance under repeated charge-discharge conditions. To systematically investigate the electrochemical properties of NMO, the MnO_2 nanorods were directly annealed at 200 °C under a N_2 atmosphere to isolate the influence of oxygen vacancies, with the resulting sample denoted as Ov-MnO_2. It can be observed that Ov-MnO_2 exhibited a similar cycling performance to MnO_2 in Fig. S9 in the ESM, with a faster decrease in capacity, which was principally ascribed to the excess oxygen vacancies by prolonged annealing. For long cycling tests at 1 A·g^{-1}, the as-prepared NMO electrode delivered prominent cycling stability. After activation, the capacity of NMO increased after the 105 cycles in Fig. 3(e), indicating that NMO was more electrochemically active than MnO_2. After 1600 cycles, the NMO cathode retained a specific capacity of 83.1 mAh·g^{-1}, demonstrating higher capacity than MnO_2 (48.2 mAh·g^{-1} after the 100 cycles), indicating that NMO possessed high structural stability for Zn^{2+} storage. Compared with other modification strategies, this work effectively enhanced the electrochemical stability of MnO_2 in Fig. S10 in the ESM.

To systematically analyze the structural evolution of N-doped MnO_2 electrodes (Fig. 4(a)), *ex-situ* XRD test across distinct charge/discharge states at 0.1 A·g^{-1} was performed.

Figure 4(b) demonstrates the phase evolution of the NMO electrode during cycling at the current density of 0.1 A·g^{-1}. Upon the first complete discharge to 0.9 V, *ex-situ* XRD measurements revealed the appearance of novel diffraction peaks at 16.2° and 32.9°, which were labeled $Zn_4SO_4(OH)_6{\cdot}H_2O$ (denoted ZHS, PDF#39-0690) and tunnel-type $ZnMn_2O_4$ (PDF#24-1133), respectively [55, 56]. The peak at 21.1° were assigned to the MnOOH (PDF#12-0733). A reversible displacement of the (310) diffraction peak for the NMO cathode is illustrated in Fig. 4(c) throughout battery cycling. This represented an invertible change of the NMO tunnel constitution due to disembedding of H^+ and Zn^{2+}. This phenomenon raised from the incorporation of H^+ and Zn^{2+} within the cathode structure as the battery discharges. Therefore, the nucleation and growth of by-products were driven by the local stacking of OH^- at the electrolyte/NMO interphase layer. The phase change process can be expressed as follows [19, 23, 55]:

Anode:

$$Zn - 2e^- \leftrightarrow Zn^{2+} \quad (1)$$

Cathode:

$$MnO_2 + H_2O + 1e^- \leftrightarrow MnOOH + OH^- \quad (2)$$

$$4Zn^{2+} + 6OH^- + SO_4^{2-} + H_2O \leftrightarrow Zn_4SO_4(OH)_6 \cdot (H_2O) \quad (3)$$

$$2MnO_2 + Zn^{2+} + 2e^- \leftrightarrow ZnMn_2O_4 \quad (4)$$

Mechanistic analysis revealed that redox coupling between metastable Mn^{3+} and Zn^{2+} under the single-electron transfer mechanism the growth of a layered $Zn_4SO_4(OH)_6{\cdot}H_2O$ phase (Fig. 4(d)) [36, 55, 57]. As shown in Figs. 4(e)–4(g), the SEM images primarily display the morphological changes on the NMO electrode surface under different charging and discharging conditions. When discharged to 0.9 V, as shown in Fig. 4(e), the formation of side products, such as nanosheets, could be observed, where the side products adhered to the surface of the nanorods. When the NMO electrode was charged to 1.8 V, a small amount of side products was still present at the surface of the positive electrode sheet, but the material retained its relatively intact nanorod morphology, demonstrating the reversibility of the electrode cycle. Under the cycling process, the near-vanishing of $Zn_4SO_4(OH)_6{\cdot}H_2O$ nanosheets from the surface of the NMO electrode matched the XRD result, reflecting the high reversibility of the material. Based on the repeated embedding and extraction of Zn^{2+} and H^+ during the cycle, NMO electrodes could maintain a good nanostructure, further proving the reversibility and stability of NMO cathode materials during the cycle. *Ex-situ* TEM and

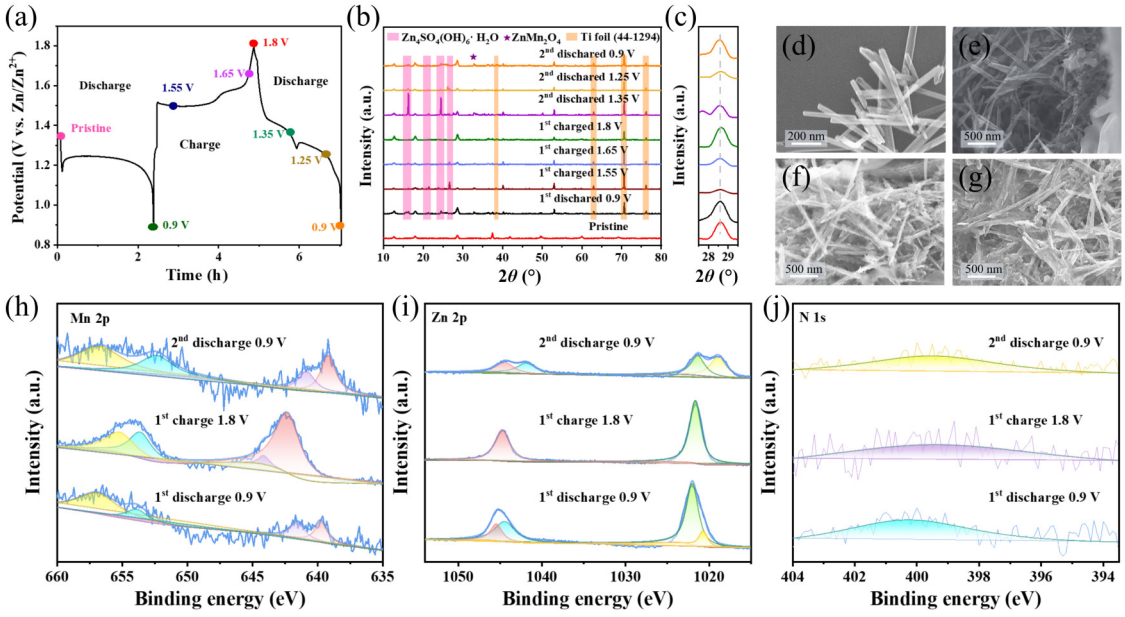

Figure 4 Analysis of the mechanism. (a) *Ex-situ* characterization of NMO electrodes under fixed conditions. (b) *Ex-situ* XRD obtained for the NMO electrode throughout the cycling process. (c) XRD pattern of NMO (310) plane. (d)–(g) Initial state, 1st discharged 0.9 V, 1st charged 1.8 V, 2nd discharged 0.9 V. (h)–(j) *Ex-situ* XPS spectra of the NMO electrode under distinct charge/discharge states.

XPS analyses were systematically conducted to corroborate the reaction mechanism and verify the structural reversibility during cycling. When discharged to 0.9 V, Figs. S11(a)–S11(d) in the ESM reveal the presence of by-products attached to the NMO surface, with lattice spacing measurements corresponding to these secondary phases. Upon charging to 1.8 V (Figs. S11(e)–S11(h) in the ESM), a small amount of residual by-products remained on the electrode surface; however, the nanorod morphology was well preserved. When the battery was discharged again to 0.9 V (Figs. S11(i)–S11(l) in the ESM), the re-emergence of by-products was observed. The *ex-situ* TEM characterization of the cycled electrode confirmed the reversibility of the NMO electrode. In the Mn 2p spectra of Fig. 4(h), the predominant presence of Mn^{3+} species is observed at the discharged state (0.9 V), while Mn^{4+} becomes dominant upon charging to 1.8 V [55–57]. Concurrently, the reduced binding energy of Zn 2p peaks in Fig. 4(i) suggested reversible decomposition of $Zn_4SO_4(OH)_6{\cdot}H_2O$ byproducts [55, 58]. The minor variations in peak intensity and position of the N 1s signal (Fig. 4(j)) indicated structural stabilization through nitrogen doping, effectively mitigating volume expansion during cycling [19, 40, 43]. As shown in Fig. S12(a) in the ESM, the decrease in the Mn–O bond implied that Mn^{4+} decreased, consistent with the former characterization [50, 54]. Additionally, the change in splitting energy of Mn corresponded to the valence state change of Mn (Mn^{4+} to Mn^{3+}/Mn^{2+}), aligning with cathodic reaction mechanisms (Fig. S12(b) in the ESM) [50, 58]. The clear emergency of Zn 3p peak corresponded the appearance of $Zn_4SO_4(OH)_6{\cdot}H_2O$ byproduct.

To further clarify the dynamics of NMO reactions, the CV of NMO and MnO_2 were tested at different scan rates in Fig. 5(a) and Fig. S13 in the ESM. Upon increasing the scanning rate, the oxidation and reduction peaks exhibited progressive broadening, but they all still retained their inherent voltammetric morphology. The voltammetric response correlation between the peak current and the CV scan rate could be revealed through this formula [55, 58, 59]:

$$i = av^b \tag{5}$$

The empirical parameters a and b can be obtained through equation fitting. When b approached 1, the battery's operation could be predominantly governed via capacitive control. In contrast, when b approximated 0.5, it signified the predominance of diffusion-controlled kinetics in the electrochemical process [60]. Figure 5(b) shows the NMO electrode material corresponding to Peak 1–4. The corresponding values of b were 0.50, 0.56, 0.76, and 0.51, respectively, which indicated that the NMO oxidation reduction involves both diffusion and capacitance processes. To quantify the capacitive behavior within the overall energy storage process, the following formula was used to calculate the capacitive contribution [54, 58, 61]:

$$i = k_1 v + k_2 v^{1/2} \tag{6}$$

Figure 5(c) shows that the capacitive contribution of NMO at 0.2 $mV{\cdot}s^{-1}$ reaches 57.6%. The contribution made by capacitance constitutes 85.2%, which was higher than the capacitive contribution of MnO_2 at 1 $mV{\cdot}s^{-1}$ (Fig. 5(d)). The diffusion-controlled kinetics result demonstrated that nitrogen-doped MnO_2 enhances capacitive charge storage through optimized electron delocalization, thereby facilitating interfacial.

Galvanostatic intermittent titration technique characterizations were systematically investigated to compare their ionic diffusion dynamics of as-prepared NMO and MnO_2 samples, revealing kinetic disparities induced by nitrogen doping [19, 62]. Figures 5(e) and 5(f) clearly represent the diffusion coefficient of Zn^{2+} ($D_{Zn^{2+}}$) obtained via this subsequent formula:

$$D_{Zn^{2+}} = \frac{4}{\pi\tau}\left(\frac{m_B V_M}{M_B S}\right)^2\left(\frac{\Delta E_s}{\Delta E_\tau}\right)^2 \tag{7}$$

Here, the key parameters were defined as: τ (the duration of the constant current pulse), m_B (weight of active material), M_B (molar mass of NMO), V_M (molar volume), and S (electrode-electrolyte interfacial area), ΔE_s / ΔE_τ (changes of voltage at different states), respectively [58, 62, 63]. The mobility of Zn^{2+} was determined by the interaction of Zn^{2+} with oxygen atoms. The lower electronegativity of N atoms compared to O atoms facilitates weakened ion-lattice interactions, which directly diminished the

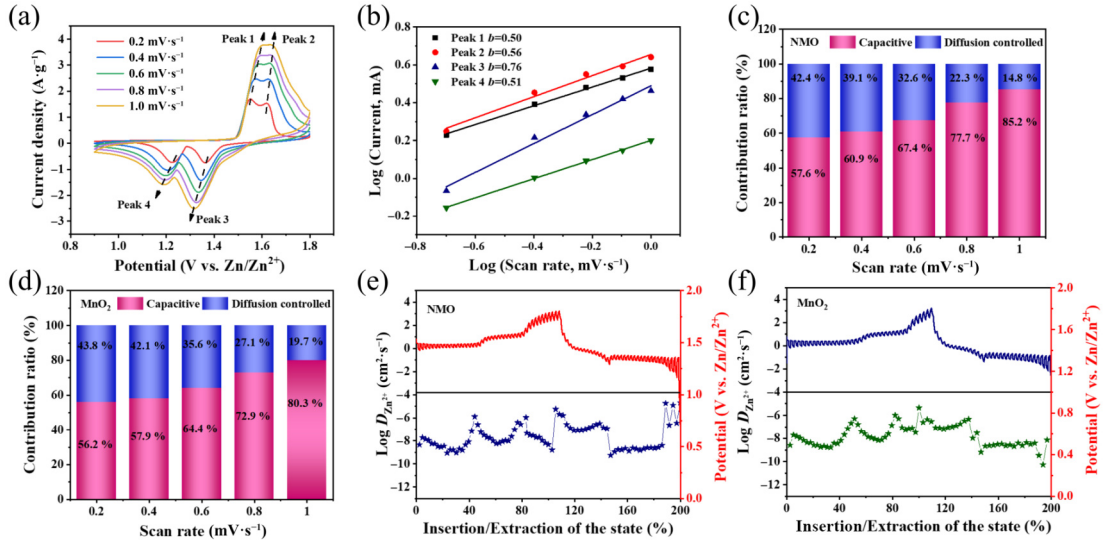

Figure 5 (a) The voltammetric response of the NMO electrode. (b) Fitting data of the log (*i*) vs. log (*v*) for the NMO electrode. The percent of pseudocapacitive contribution for NMO (c) and MnO_2 (d) electrodes. The result of Zn^{2+} diffusion kinetics of NMO (e) and MnO_2 (f) electrodes.

energybarrierforiondiffusion.TheionicdiffusionofNMOwas2.0×10^{-5}to 9.3×10^{-10} cm^2·s^{-1}, larger than that of pure MnO_2 (4.4×10^{-6} to 5.3×10^{-11} cm^2·s^{-1}); it favored the adsorption and desorption of Zn^{2+} at the surface of the cathode material, implying faster ion diffusion kinetics. A comprehensive comparison of NMO demonstrated that NMO possessed a range of superior properties for battery application.

4 Conclusions

In this work, we proposed that nitrogen doping in MnO_2 through low-temperature annealing can effectively construct NMO cathode materials that enhancing the ion diffusion rate and cycling stability. Electrochemical analysis showed that N atoms with low electronegativity could weaken the interaction between the host ion and cathode material, thereby strengthening the reaction kinetics of Mn^{4+}/Mn^{3+} in Zn-NMO batteries. The NMO cathode demonstrated enhanced electrochemical performance relative to MnO_2, exhibiting lower charge-transfer impedance, faster Zn^{2+} diffusion, and higher electrochemical activity. Through the electrochemical performance measurements, NMO exhibited higher specific capacitance of 290.8, 242.2, and 210.3 mAh·g^{-1} at 0.1, 1, and 2 A·g^{-1}, respectively. In contrast, the discharge capacity of NMO after 1600 cycles at 1 A·g^{-1} could still retain a high specific capacity of 82.7 mAh·g^{-1}. In addition, the energy storage mechanism of the Zn-NMO battery was studied deeply, which suggested nitrogen doping can effectively enhance H^+/Zn^{2+} insertion. This nitrogen doping could provide a holistic approach to cathode material design, which can synergistically enhance cathode-specific capacity and structural integrity in aqueous zinc-based battery systems.

Acknowledgements

The research is supported by the following funding programs: Natural Science Research Project of Jiangsu Higher Education Institutions of China (23KJB430029) and the National Natural Science Foundation of China (52402198); Jiangsu Provincial Department of Science and Technology (BK20240821 and BK20232041); International Joint Laboratory on Low-Dimensional Optoelectronic Materials and Devices of Soochow University and Suzhou Foreign Academician Workstation.

Declaration of conflicting interests

The authors declare no conflicting interests regarding the content of this article.

Data availability

All data needed to support the conclusions in the paper are presented in the manuscript and/or the Supplementary Materials. Additional data related to this paper may be requested from the corresponding author upon request.

Electronic Supplementary Material: Supplementary material (detailed data about XRD, SEM, HRTEM, EDS, XPS, CV, and battery cycling) is available in the online version of this article at https://doi.org/10.26599/NRE.2025.9120182.

References

[1] Dunn, B.; Kamath, H.; Tarascon, J. M. Electrical energy storage for the grid: A battery of choices. *Science* **2011**, *334*, 928–935.

[2] Qiu, B.; Zhang, M. H.; Wu, L. J.; Wang, J.; Xia, Y. G.; Qian, D. N.; Liu, H. D.; Hy, S.; Chen, Y.; An, K. et al. Gas-solid interfacial modification of oxygen activity in layered oxide cathodes for lithium-ion batteries. *Nat. Commun.* **2016**, *7*, 12108.

[3] Liu, B. W.; Hu, N. F.; Li, C.; Ma, J.; Zhang, J. W.; Yang, Y.; Sun, D. Y.; Yin, B. X.; Cui, G. L. Direct observation of Li-ion transport heterogeneity induced by nanoscale phase separation in Li-rich cathodes of solid-state batteries. *Angew. Chem., Int. Ed.* **2022**, *61*, e202209626.

[4] Huang, W. Y.; Li, J. Y.; Zhao, Q. H.; Li, S. N.; Ge, M. Y.; Fang, J. J.; Chen, Z. F.; Yu, L.; Huang, X. Z.; Zhao, W. G. et al. Mechanochemically robust $LiCoO_2$ with ultrahigh capacity and prolonged cyclability. *Adv. Mater.* **2024**, *36*, e2405519.

[5] Jia, H.; Yang, Z. J.; Xu, Y. B.; Gao, P. Y.; Zhong, L. R.; Kautz, D. J.; Wu, D. G.; Fliegler, B.; Engelhard, M. H.; Matthews, B. E. et al. Is nonflammability of electrolyte overrated in the overall safety performance of lithium ion batteries? A sobering revelation from a completely nonflammable electrolyte. *Adv. Energy Mater.* **2023**, *13*, 2203144.

[6] Ren, Y. J.; Zhang, S. W.; Yin, B. S.; Loh, J. R.; Ding, Y. X.; Huang, X. J.; Li, J. Z.; Li, H.; Ma, T. Y. Boosting the stability of highly flexible cathodes in zinc-ion batteries via the pillaring effect of molybdenum in α-MnO_2. *Batteries Supercaps* **2023**, *6*, e202300132.

[7] Zhu, C. Y.; Li, P. Z.; Xu, G. Y.; Cheng, H.; Gao, G. Recent progress

and challenges of Zn anode modification materials in aqueous Zn-ion batteries. *Coord. Chem. Rev.* **2023**, *485*, 215142.
[8] Liu, Y. Z.; Qin, Z. M.; Yang, X. P.; Liu, J.; Liu, X. X.; Sun, X. Q. Voltage induced lattice contraction enabling superior cycling stability of MnO_2 cathode in aqueous zinc batteries. *Energy Storage Mater.* **2023**, *56*, 524–531.
[9] Liu, Y. Z.; Wang, K.; Yang, X. P.; Liu, J.; Liu, X. X.; Sun, X. Q. Enhancing two-electron reaction contribution in MnO_2 cathode material by structural engineering for stable cycling in aqueous Zn batteries. *ACS Nano* **2023**, *17*, 14792–14799.
[10] Jiang, N.; Zeng, Y.; Yang, Q.; Lu, P. D.; Qu, K. Q.; Ye, L. H.; Lu, X. J.; Liu, Z. Q.; Li, X. X.; Tang, Y. C. et al. Deep ion mass transfer addressing the capacity shrink challenge of aqueous Zn‖MnO_2 batteries during the cathode scaleup. *Energy Environ. Sci.* **2024**, *17*, 8904–8914.
[11] Zhao, Y.; Zhou, R. K.; Song, Z. H.; Zhang, X. D.; Zhang, T.; Zhou, A. B.; Wu, F.; Chen, R. J.; Li, L. Interfacial designing of MnO_2 half-wrapped by aromatic polymers for high-performance aqueous zinc-ion batteries. *Angew. Chem., Int. Ed.* **2022**, *61*, e202212231.
[12] Zhang, A. Q.; Zhao, R.; Wang, Y. H.; Yue, J. S.; Yang, J. J.; Wang, X. R.; Wu, C.; Bai, Y. Hybrid superlattice-triggered selective proton Grotthuss intercalation in δ-MnO_2 for high-performance zinc-ion battery. *Angew. Chem., Int. Ed.* **2023**, *62*, e202313163.
[13] Wang, D. H.; Wang, L. F.; Liang, G. J.; Li, H. F.; Liu, Z. X.; Tang, Z. J.; Liang, J. B.; Zhi, C. Y. A superior δ-MnO_2 cathode and a self-healing Zn-δ-MnO_2 battery. *ACS Nano* **2019**, *13*, 10643–10652.
[14] Shi, H. Y.; Ye, Y. J.; Liu, K.; Song, Y.; Sun, X. Q. A long-cycle-life self-doped polyaniline cathode for rechargeable aqueous zinc batteries. *Angew. Chem., Int. Ed.* **2018**, *57*, 16359–16363.
[15] Ding, J. W.; Zheng, H. Y.; Gao, H. G.; Liu, Q. N.; Hu, Z.; Han, L. F.; Wang, S. W.; Wu, S. D.; Fang, S. M.; Chou, S. L. *In situ* lattice tunnel distortion of vanadium trioxide for enhancing zinc ion storage. *Adv. Energy Mater.* **2021**, *11*, 2100973.
[16] Wang, W. F.; Zhang, L.; Duan, Z. A.; Li, R. Y.; Zhao, J. J.; Tang, L. T.; Sui, Y.; Qi, Y. D.; Han, S. M.; Fang, C. et al. Joint cationic and anionic redox chemistry in a vanadium oxide cathode for zinc batteries achieving high energy density. *Carbon Energy* **2024**, *6*, e577.
[17] Yang, Q.; Mo, F. N.; Liu, Z. X.; Ma, L. T.; Li, X. L.; Fang, D. L.; Chen, S. M.; Zhang, S. J.; Zhi, C. Y. Activating C-coordinated iron of iron hexacyanoferrate for Zn hybrid-ion batteries with 10000-cycle lifespan and superior rate capability. *Adv. Mater.* **2019**, *31*, 1901521.
[18] Housel, L. M.; Wang, L.; Abraham, A.; Huang, J. P.; Renderos, G. D.; Quilty, C. D.; Brady, A. B.; Marschilok, A. C.; Takeuchi, K. J.; Takeuchi, E. S. Investigation of α-MnO_2 tunneled structures as model cation hosts for energy storage. *Acc. Chem. Res.* **2018**, *51*, 575–582.
[19] Li, G. J.; Sun, L.; Zhang, S. L.; Zhang, C. F.; Jin, H. Y.; Davey, K.; Liang, G. M.; Liu, S. L.; Mao, J. F.; Guo, Z. P. Developing cathode materials for aqueous zinc ion batteries: Challenges and practical prospects. *Adv. Funct. Mater.* **2024**, *34*, 2301291.
[20] Li, Y.; Li, X.; Duan, H.; Xie, S. Y.; Dai, R. Y.; Rong, J. H.; Kang, F. Y.; Dong, L. B. Aerogel-structured MnO_2 cathode assembled by defect-rich ultrathin nanosheets for zinc-ion batteries. *Chem. Eng. J.* **2022**, *441*, 136008.
[21] Zheng, J. J.; Qin, C. C.; Chen, C.; Zhang, C. K.; Shi, P.; Chen, X.; Gan, Y.; Li, J. Y.; Yao, J.; Liu, X. et al. Ostwald ripening mechanism-derived MnOOH induces lattice oxygen escape for efficient aqueous MnO_2–Zn batteries. *J. Mater. Chem. A* **2023**, *11*, 24311–24320.
[22] Zhao, Q. H.; Song, A. Y.; Ding, S. X.; Qin, R. Z.; Cui, Y. H.; Li, S. N.; Pan, F. Preintercalation strategy in manganese oxides for electrochemical energy storage: Review and prospects. *Adv. Mater.* **2020**, *32*, 2002450.
[23] Li, Q. G.; Wang, C.; Zhu, Y.; Du, W. Z.; Liu, W. X.; Yao, M.; Wang, Y. Q.; Qian, Y. M.; Feng, S. J. Unlocking the critical role of Mg doping in α-MnO_2 cathode for aqueous zinc ion batteries. *Chem. Eng. J.* **2024**, *485*, 150077.
[24] Zhang, Q.; Fan, H. F.; Liu, Q. F.; Wu, Y. G.; Wang, E. D. Fe-doped α-MnO_2/rGO cathode material for zinc ion batteries with long lifespan and high areal capacity. *J. Mater. Chem. A* **2024**, *12*, 8167–8174.
[25] Zhao, Y. J.; Zhang, S. X.; Zhang, Y. Y.; Liang, J. R.; Ren, L. T.; Fan, H. J.; Liu, W.; Sun, X. M. Vacancy-rich Al-doped MnO_2 cathodes break the trade-off between kinetics and stability for high-performance aqueous Zn-ion batteries. *Energy Environ. Sci.* **2024**, *17*, 1279–1290.
[26] Li, Y.; Liu, X. X.; Ji, T. Y.; Zhang, M.; Yan, X. R.; Yao, M. J.; Sheng, D. W.; Li, S. D.; Ren, P. P.; Shen, Z. X. Potassium ion doped manganese oxide nanoscrolls enhanced the performance of aqueous zinc-ion batteries. *Chin. Chem. Lett.* **2025**, *36*, 109551.
[27] Lan, R.; Gkanas, E.; Sahib, A. J. S.; Greszta, A.; Bhagat, R.; Roberts, A. The effect of copper doping in α-MnO_2 as cathode material for aqueous zinc-ion batteries. *J. Alloy. Compd.* **2024**, *992*, 174528.
[28] Lin, M. X.; Shao, F. Q.; Tang, Y.; Lin, H. J.; Xu, Y. C.; Jiao, Y.; Chen, J. R. Layered Co doped MnO_2 with abundant oxygen defects to boost aqueous zinc-ion storage. *J. Colloid Interf. Sci.* **2022**, *611*, 662–669.
[29] Xia, X. Y.; Zhao, Y. J.; Zhao, Y.; Xu, M. G.; Liu, W.; Sun, X. M. Mo doping provokes two electron reaction in MnO_2 with ultrahigh capacity for aqueous zinc ion batteries. *Nano Res.* **2023**, *16*, 2511–2518.
[30] Zhao, Q. H.; Song, A. Y.; Zhao, W. G.; Qin, R. Z.; Ding, S. X.; Chen, X.; Song, Y. L.; Yang, L. Y.; Lin, H.; Li, S. N. et al. Boosting the energy density of aqueous batteries via facile Grotthuss proton transport. *Angew. Chem., Int. Ed.* **2021**, *60*, 4169–4174.
[31] Wang, M.; Zhao, G. Y.; Bai, X. M.; Yu, W. J.; Zhao, C. H.; Gao, Z. R.; Lyu, P. B.; Chen, Z. Y.; Zhang, N. Q. Gradient concentration refilling of N stabilizes oxygen vacancies for enhanced Zn^{2+} storage. *Adv. Energy Mater.* **2023**, *13*, 2301730.
[32] Song, Q. Y.; Zhou, S. H.; Wang, S. Y.; Li, S.; Xu, L.; Qiu, J. X. Insights into the oxygen vacancies in transition metal oxides for aqueous zinc-ion batteries. *Chem. Eng. J.* **2023**, *461*, 142033.
[33] Abdelmohsen, A. H.; El-Khodary, S. A.; Ismail, N.; Song, Z. L.; Lian, J. B. Basics and advances of manganese-based cathode materials for aqueous zinc-ion batteries. *Chem. -Eur. J.* **2025**, *31*, e202403425.
[34] Xie, D. M.; Wang, Y.; Tian, L. W.; Huang, H. J.; Sun, J. Y.; Kim, D. W.; Zhao, J. C.; Mao, J. F. Dual-functional Ca-ion-doped layered δ-MnO_2 cathode for high-performance aqueous zinc-ion batteries. *Adv. Funct. Mater.* **2025**, *35*, 2413993.
[35] Lin, M. X.; Shao, F. Q.; Weng, S. T.; Xiong, S. S.; Liu, S.; Jiang, S. Y.; Xu, Y. C.; Jiao, Y.; Chen, J. R. Boosted charge transfer in oxygen vacancy-rich K^+ birnessite MnO_2 for water oxidation and zinc-ion batteries. *Electrochim. Acta* **2021**, *378*, 138147.
[36] Zhang, X.; Ma, X. L.; Bi, H. L.; Zhang, Y. F.; Mi, P. P.; Liu, F. R.; Jin, X. C.; Chen, Y.; Zhang, K.; Wang, J. et al. Carboxymethylcellulose induced the formation of amorphous MnO_2 nanosheets with abundant oxygen vacancies for fast ion diffusion in aqueous zinc-ion batteries. *Adv. Funct. Mater.* **2025**, *35*, 2411990.
[37] Zhou, X. Z.; Li, X. Y.; Pang, J. J.; Lei, Z. Q. Recent progress on modification strategies of both metal zinc anode and manganese dioxide cathode materials for high-performance aqueous zinc-ion batteries. *Coordin. Chem. Rev.* **2025**, *523*, 216255.
[38] Cui, Z. B.; Li, Q. Z.; Li, S. R.; Zheng, W. J.; Li, X. H.; Shu, D.; Yuan, L. B.; Lu, J. C.; Cheng, H. H.; Meng, T. Nickel-doping induced oxygen vacancies in MnO_2 hollow cube with enlarged interlayer spacing for stable sodium ions storage. *Small* **2025**, *21*, 2410766.
[39] Xie, M.; Lin, M. X.; Feng, C.; Liu, Z. J.; Xu, Y. C.; Wang, N. N.; Zhang, X.; Jiang, Y.; Chen, J. R. Coupling Zn^{2+} doping and rich oxygen vacancies in MnO_2 nanowire toward advanced aqueous zinc-ion batteries. *J. Colloid Interf. Sci.* **2023**, *645*, 400–409.
[40] Zhang, Z. N.; Li, S.; Zhao, B.; Zhang, X. L.; Wang, X. Y.; Wen, Z. S.; Ji, S. J.; Sun, J. C. Joint influence of nitrogen doping and oxygen vacancy on manganese dioxide as a high-capacity cathode for zinc-ion batteries. *J. Phys. Chem. C* **2021**, *125*, 20195–20203.
[41] Zhao, Y. J.; Zhang, P. J.; Liang, J. R.; Xia, X. Y.; Ren, L. T.; Song, L.; Liu, W.; Sun, X. M. Uncovering sulfur doping effect in MnO_2 nanosheets as an efficient cathode for aqueous zinc ion battery. *Energy Storage Mater.* **2022**, *47*, 424–433.
[42] Xiong, T.; Zhang, Y. X.; Lee, W. S. V.; Xue, J. M. Defect engineering in manganese-based oxides for aqueous rechargeable zinc-ion batteries: A review. *Adv. Energy Mater.* **2020**, *10*, 2001769.

[43] Ye, H. J.; Zeng, X. M.; Li, X. M.; He, K.; Li, Y. S.; Yuan, Y. F. Review of ion doping and intercalation strategies for advancing manganese-based oxide cathodes in aqueous zinc-ion batteries. *Nano Energy* **2025**, *136*, 110740.
[44] Choudhary, D.; Bala, R.; Shrivastav, M.; Dhiman, R. MnO_2/rGO bifunctional catalyst and support materials for gel polymer electrolyte based Zn-air batteries. *Electrochim. Acta* **2024**, *507*, 145179.
[45] Liang, J. R.; Zhao, Y. J.; Ren, L. T.; Li, M. C.; Zhang, Q. L.; Wang, Y. H.; Sun, X. M.; Chuai, M. Y.; Wang, X. S.; Liu, W. Dual anions doping enhanced conductivity and stability of layered δ-MnO_2 cathode for aqueous zinc-ion battery. *Adv. Funct. Mater.* **2025**, *35*, 2501135.
[46] Ma, K. X.; Ge, S. Y.; Fu, R. R.; Feng, C. H.; Zhao, H. Y.; Shen, X. R.; Liang, G. F.; Zhao, Y.; Jiao, Q. Z. Uncovering Se, P co-doping effect in MnO_2 toward high-performance aqueous zinc-ion batteries. *Chem. -Eur. J.* **2024**, *484*, 149525.
[47] Chen, J. Y.; Liang, J. X.; Zhou, Y.; Sha, Z.; Lim, S.; Huang, F.; Han, Z. J.; Brown, S. A.; Cao, L. Y.; Wang, D. W.; Wang, C. H. A vertical graphene enhanced Zn–MnO_2 flexible battery towards wearable electronic devices. *J. Mater. Chem. A* **2021**, *9*, 575–584.
[48] Wang, X. B.; Hu, J. J.; Liu, W. D.; Wang, G. Y.; An, J.; Lian, J. S. Ni–Zn binary system hydroxide, oxide and sulfide materials: Synthesis and high supercapacitor performance. *J. Mater. Chem. A* **2015**, *3*, 23333–23344.
[49] Yao, H. X.; Yu, H.; Zheng, Y. Q.; Li, N. W.; Li, S.; Luan, D. Y.; Lou, X. W.; Yu, L. Pre-intercalation of ammonium ions in layered δ-MnO_2 nanosheets for high-performance aqueous zinc-ion batteries. *Angew. Chem., Int. Ed.* **2023**, *62*, e202315257.
[50] Dai, L. X.; Wang, Y.; Sun, L.; Ding, Y.; Yao, Y. Q.; Yao, L. D.; Drewett, N. E.; Zhang, W.; Tang, J.; Zheng, W. T. Jahn-teller distortion induced Mn^{2+}-rich cathode enables optimal flexible aqueous high-voltage Zn–Mn batteries. *Adv. Sci.* **2021**, *8*, 2004995.
[51] He, T. H.; Zeng, X. S.; Rong, S. P. The controllable synthesis of substitutional and interstitial nitrogen-doped manganese dioxide: The effects of doping sites on enhancing the catalytic activity. *J. Mater. Chem. A* **2020**, *8*, 8383–8396.
[52] Liu, Y.; Zhang, S. Q.; Ma, S. K.; Sun, X. Y.; Wang, Y.; Liu, F.; Li, Y.; Ma, Y. H.; Xu, X. W.; Xue, Y. M. et al. Electronic structure modification of MnO_2 nanosheet arrays with enhanced water oxidation activity and stability by nitrogen plasma. *ACS Appl. Mater. Interfaces* **2024**, *16*, 36498–36508.
[53] Yu, P. F.; Zhou, J. X.; Zheng, M. T.; Li, M. R.; Hu, H.; Xiao, Y.; Liu, Y. L.; Liang, Y. R. Boosting zinc ion energy storage capability of inert MnO cathode by defect engineering. *J. Colloid Interf. Sci.* **2021**, *594*, 540–549.
[54] Zhang, Y.; Deng, S. J.; Luo, M.; Pan, G. X.; Zeng, Y. X.; Lu, X. H.; Ai, C. Z.; Liu, Q.; Xiong, Q. Q.; Wang, X. L. et al. Defect promoted capacity and durability of N–MnO_{2-x} branch arrays via low-temperature NH_3 treatment for advanced aqueous zinc ion batteries. *Small* **2019**, *15*, 1905452.
[55] Karbak, M.; Baazizi, M.; Sayah, S.; Autret-Lambert, C.; Tison, Y.; Martinez, H.; Chafik, T.; Ghamouss, F. Unraveling high-performance oxygen-deficient amorphous manganese oxide as the cathode for advanced zinc ion batteries. *J. Mater. Chem. A* **2023**, *11*, 2634–2640.
[56] Wang, G.; Wang, Y.; Guan, B.; Liu, J.; Zhang, Y.; Shi, X.; Tang, C.; Li, G.; Li, Y.; Wang, X. et al. Hierarchical K-birnessite-MnO_2 carbon framework for high-energy-density and durable aqueous zinc-ion battery. *Small* **2021**, *17*, 2104557.
[57] Zhang, Q.; Zhao, J.; Chen, X.; Yang, R.; Ying, T.; Cheng, C.; Liu, B.; Fan, J.; Li, S.; Zeng, Z. Unveiling the energy storage mechanism of MnO_2 polymorphs for zinc-manganese dioxide batteries. *Adv. Funct. Mater.* **2024**, *34*, 2306652.
[58] Xu, P.; Yi, H. M.; Shi, G. J.; Xiong, Z. N.; Hu, Y. Y.; Wang, R. L.; Zhang, H. H.; Wang, B. F. Mg ion pre-intercalated MnO_2 nanospheres as high-performance cathode materials for aqueous Zn-ion batteries. *Dalton Trans.* **2022**, *51*, 4695–4703.
[59] Liu, W. J.; Qiao, F.; Zhao, J. K. Tuning electrochemical properties of carbon nanofiber electrodes with selenium heteroatoms for flexible zinc ion capacitors. *Nano Res. Energy* **2024**, *3*, e9120131.
[60] Wang, J. L.; Gao, X. Y.; Wang, Y. W.; Pan, R. N.; Liu, Z.; Liu, X.; Xie, H. J.; Yu, F.; Wang, G.; Gu, T. T. Robust ring insoluble naphthoquinone derivative cathode with high loading and long cycle life for aqueous zinc organic batteries. *Nano Res. Energy* **2024**, *3*, e9120124.
[61] Lu, Y. N.; Wang, T. L.; Naresh, N.; Borowiec, J.; Parkin, I. P.; Boruah, B. D. Pre-doped cations in V_2O_5 for high-performance Zn-ion batteries. *Nano Res. Energy* **2024**, *3*, e9120125.
[62] Li, G. M.; Yu, W. J.; Diao, Q. Q.; Zhang, Y. T.; Tang, F.; Luo, X. L.; Yan, L. T.; Zhao, X. B.; Li, G. D. Zn-doped hollow cubic MnO_2 as a high-performance cathode material for Zn ion batteries. *ChemPhysChem* **2025**, *26*, e202400860.
[63] Fu, Y. C.; Jia, C. E.; Chen, Z. H.; Zhang, X. S.; Liang, S. J.; Zhai, Z.; Chen, J. Z.; Liu, X. Y.; Zhang, L. L. Modulating residual ammonium in MnO_2 for high-rate aqueous zinc-ion batteries. *Nanoscale* **2022**, *14*, 3242–3249.

Huiying Gao is a postgraduate student in the School of Physical Science and Technology, Soochow University. Her main research interest is the modification of the cathode for aqueous zinc-ion batteries.

Qi Xue is a lecturer at the School of Physical Science and Technology, Soochow University. Her research focuses on multifunctional nanomaterials and applications in energy storage/optoelectronic devices.